Code Calibration Program in Support of the Aeroassist Flight Experiment

Peter A. Gnoffo*
NASA Langley Research Center, Hampton, Virginia 23665

The code calibration program for the Langley Aerothermodynamic Upwind Relaxation Algorithm (LAURA) is reviewed with the emphasis directed toward support of the Aeroassist Flight Experiment (AFE). The flight project is designed to obtain data that will be used in the validation of computational fluid dynamic approximation methods. Comparisons between experimental data and numerical simulation focus on perfect-gas tests over a scale model of the AFE and on flight and ground tests that challenge some aspect of the thermochemical nonequilibrium model. In the first case, the gas model is simple, but the grid-related problems of defining the real vehicle are present. In the second case, the vehicle geometries are simple, but thermochemical processes must be modeled correctly to compare with the experimental data. These comparisons are described as calibration runs because they test elements of the numerical simulation, but no single data set adequately simulates the full-scale AFE flight conditions. Comparisons between computation and experiment over a broad range of data sets show generally good agreement, though some aspects of the numerical model require further development. Recent developments in a computational singular perturbation procedure, used to identify critical reactions in the chemical kinetic model, are also discussed.

Nomenclature

C_H = heat-transfer coefficient
$C_{H,FR}$ = theoretical reference heat-transfer coefficient
C_p = pressure coefficient
C_r = leading factor of expression for reaction rate coefficient
c_s = mass fraction species s
D_s = effective diffusion coefficient for species s
E = total energy per unit mass of mixture
e_v = vibrational-electronic energy per unit mass of gas mixture
F = fringe number
g = inviscid component of flux vector relative to cell face
H = total enthalpy per unit mass of mixture
h = viscous component of flux vector relative to cell face
h_s = enthalpy per unit mass of species s
$h_{V,s}$ = vibrational-electronic enthalpy per unit mass of species s
$k_{f,r}$ = forward reaction rate coefficient for reaction r
L = geometric path length of interferogram
N_e = electron number density
n_x, n_y, n_z = components of unit vector normal to finite-volume cell face
p = pressure
Q_{rad} = radiative energy transfer rate
q = heat-transfer rate
q = vector of conserved variables
R = radius of model
s = arc length
T = translational-rotational temperature
T_V = vibrational-electron-electronic excitation temperature
T_d = rate controlling temperature for dissociative reactions
t = time
U = velocity component in direction normal to finite-volume cell face
V_∞ = freestream velocity
$\dot{w}_s$ = mass production rate of species s per unit volume
$\dot{w}_v$ = vibrational-electronic energy source term
x,y,z = Cartesian coordinates
y_s = mole fraction of species s
α = angle of attack
δ = forward difference in time, shock standoff distance
η = frozen thermal conductivity for translational and rotational energy of heavy particles
η_V = frozen thermal conductivity for vibrational-electronic energy
λ = wavelength of light in interferogram
μ = mixture viscosity
ρ = mixture density
ρ_s = density of species s
σ = cell face area
τ = shear stress
$\dot{\omega}$ = vector of source terms
Ω = cell volume

Subscripts

e = electron
I,J,K = indices of cell centers in rectangularly ordered space
i,j,k = indices of cell walls in rectangularly ordered space
L = dummy index for a cell center
l = dummy index for a cell wall
n = direction normal to cell face
r = reaction r
ref = reference quantity
s = species s
V = vibrational-electronic
∞ = freestream

Presented as Paper 89-1673 at the AIAA 24th Thermophysics Conference, Buffalo, NY, June 12-14, 1989; received July 15, 1989. Copyright © 1989 American Institute of Aeronautics and Astronautics, Inc. No copyright is asserted in the United States under Title 17, U.S. Code. The U.S. Government has a royalty-free license to exercise all rights under the copyright claimed herein for Governmental purposes. All other rights are reserved by the copyright owner.

*Aerospace Engineer, Aerothermodynamics Branch, Space Systems Division. Senior Member AIAA.

Introduction

THE Aeroassist Flight Experiment[1] (AFE) is a project designed to obtain critical flight data that will be used in the validation of computational fluid dynamic (CFD) approximation methods. These CFD codes require flight data for validation because of the complexity of the important physical processes that must be modeled to accurately predict aerody-

namic forces and convective and radiative heating for planned aeroassisted space transfer vehicles (ASTV). Typical ASTV trajectories use aerobraking and aeromaneuvering to circularize high energy entries from geosynchronous Earth orbit, from the moon, or the Mars with entry velocities ranging from 10 to 15 km/s.[2] Most of the aeroassisted maneuver takes place in the upper atmosphere with typical perigees occurring at altitudes between 60–80 km. The flow regimes range from free molecular to continuum, and nonequilibrium processes are critically important in the definition of the shock layer and base flow surrounding the brake surface and payload of an ASTV. Conventional, ground-based hypersonic facilities (i.e., wind tunnels, ballistic ranges, shock tunnels, and arc jets) provide important data used in the code calibration process but are unable to simultaneously simulate the appropriate energies and length scales encountered in full-scale ASTV flowfields. In contrast, the AFE, a heavily instrumented, blunt, raked elliptic cone with a 14-ft maximum diameter, will be launched from low Earth orbit into the atmosphere to simulate a return from geosynchronous orbit, retrieving critical validation data. (Definitions of the terms "validation" and "calibration" are somewhat subjective. Here, calibration refers to comparison of CFD prediction with experimental data that include some elements of the intended application domain, whereas validation refers to comparison of CFD prediction with experimental data that include sufficient critical elements of the intended application domain to challenge the simulation.)

The code calibration program for the Langley Aerothermodynamic Upwind Relaxation Algorithm (LAURA)[3-7] is reviewed herein, with emphasis directed toward support of the AFE in the near term and ASTV design in the long term. LAURA is an upwind-biased, point-implicit relaxation algorithm for obtaining the numerical solution to the governing equations for three-dimensional, viscous, hypersonic flows in chemical and thermal nonequilibrium. The algorithm is derived using a finite-volume formulation in which the inviscid components of flux across cell walls are described with Roe's averaging[8] and Harten's entropy fix[9] with second-order corrections based on Yee's symmetric total variation diminishing scheme.[10,11] Because of the point-implicit relaxation strategy, the algorithm remains stable at large Courant numbers without the necessity of solving large, block tridiagonal systems. More detailed information concerning the algorithm may be found in Refs. 5–7.

Predictions for pressure distributions and surface heating coefficients compare well with experimental data[12,13] for Mach 10 flow over an AFE wind-tunnel model. Predictions for the hypersonic flow of air in chemical and thermal nonequilibrium (velocity = 8917 m/s, altitude = 78 km) over the full-scale AFE configuration obtained on a multidomain grid are discussed. Comparisons with other calibration data, including the Fire II[14] and RAM-C[15] flight experiments and nonequilibrium flow over a sphere[16] and cylinder,[17] are also presented. Recent developments in a computational singular perturbation (CSP) procedure,[18-20] which can be used to identify critical reactions and to simplify the chemical kinetic model, are reviewed.

Conservation Equations

All of the equations and variables in this section have been described in Ref. 6. A brief review of the equation set is presented for the reader's convenience. The modeled system includes continuity equations for 11 species, three momentum equations, and two energy equations describing the conservation of vibrational-electronic and total energies. Species 1–5 are the neutral components of air consisting of N,O,N_2,O_2, and NO. Species 6–10 are the ions corresponding to species 1–5, in which one electron has been removed. Species 11 are the free electrons. The vibrational and electronic energies of all species are assumed to be in equilibrium at temperature T_V. The translational and rotational energies of all species are assumed to be in equilibrium at temperature T. Justification for these assumptions, which constitute a two-temperature model for thermal nonequilibrium, is discussed in Refs. 5 and 21.

The inviscid, viscous, and source-term contributions to the complete conservation laws are considered separately for convenience. Let $\boldsymbol{g}$ define the inviscid terms, $\boldsymbol{h}$ the viscous terms, and $\dot{\omega}$ the source terms. The finite-volume formulation of the conservation laws follows.

$$\left[\frac{\delta \boldsymbol{q}\Omega}{\delta t}\right]_L + \sum_{l=i,j,k} [\boldsymbol{g}_{l+1}\sigma_{l+1} - \boldsymbol{g}_l\sigma_l] + \sum_{l=i,j,k} [\boldsymbol{h}_{l+1}\sigma_{l+1} - \boldsymbol{h}_l\sigma_l] = [\dot{\omega}\Omega]_L \tag{1}$$

where

$$\boldsymbol{q} = \begin{bmatrix} \rho_s \\ \rho u \\ \rho v \\ \rho w \\ \rho E \\ \rho e_V \end{bmatrix} \tag{2}$$

$$\boldsymbol{g} = \begin{bmatrix} \rho_s U \\ \rho U u + p n_x \\ \rho U v + p n_y \\ \rho U w + p n_z \\ \rho U H \\ \rho U e_V \end{bmatrix} \tag{3}$$

$$\boldsymbol{h} = \begin{bmatrix} -\rho D_s \dfrac{\partial y_s}{\partial s_n} \\ -\tau_{nx} \\ -\tau_{ny} \\ -\tau_{nz} \\ -u\tau_{nx} - v\tau_{ny} - w\tau_{nz} - \eta \dfrac{\partial T}{\partial s_n} - \eta_V \dfrac{\partial T_V}{\partial s_n} - \rho \sum_{s=1}^{11} h_s D_s \dfrac{\partial y_s}{\partial s_n} \\ -\eta_V \dfrac{\partial T_V}{\partial s_n} - \rho \sum_{s=1}^{11} h_{V,s} D_s \dfrac{\partial y_s}{\partial s_n} \end{bmatrix} \tag{4}$$

$$\dot{\omega} = \begin{bmatrix} \dot{w}_s \\ 0 \\ 0 \\ 0 \\ Q_{\text{rad}} \\ \dot{w}_V \end{bmatrix} \tag{5}$$

The first element of the vectors defined in Eqs. (2-5) describes the species conservation; the next three elements describe x, y, and z momentum conservation; the fourth element describes total energy conservation; and the fifth element describes vibrational-electronic energy conservation. The reactive source terms for the species conservation equations are denoted by $\dot{w}_s$. The radiative energy transport term Q_{rad} may be treated as a source term in the energy equation, though its effects are not considered in the present analysis. Finally, the vibrational-electronic energy source term $\dot{w}_V$ accounts for the mechanisms by which vibrational or electronic energy is lost or gained from collisions among particles in the cell. These mechanisms include 1) the energy exchange (relaxation) between vibrational and translational modes due to collisions within the cell; 2) the vibrational energy lost or gained due to molecular depletion (dissociation) or production (recombination) in the cell; 3) the electronic-translational energy exchange due to elastic collisions between electrons and heavy particles; 4) the energy loss due to electron impact ionization; 5) the rate of energy loss due to radiation caused by electronic transitions; and 6) a term related to the work done on electrons by an electric field induced by the electron pressure gradient minus the flow work due to electron pressure. The electron pressure flow work is normally considered part of the electronic enthalpy in the inviscid (convective) portion of the flux balance. Moving the electron pressure from the convective term to the source term simplifies the expression of Jacobian eigenvalues and eigenvectors of the inviscid flux vector.

Results and Discussion

The comparisons between experimental data and numerical simulation presented herein focus on perfect-gas wind-tunnel tests over a scale model of the AFE and on both flight and ground tests that challenge some aspect of the thermochemical nonequilibrium model. In the first case, the gas model is simple, but the grid-related problems of defining the real vehicle (with the exception of some protuberances in the base region) are present. In the second case, the vehicle geometries are simple, but nonequilibrium processes must be modeled correctly in order to compare with the experimental data. These comparisons are described as calibration runs because they test elements of the numerical simulation, but no single data set adequately simulates the full-scale AFE flight conditions. In the absence of validation-quality data, these calibration data sets provide necessary, but not sufficient, checkpoints in the code validation process for aeroassisted space transfer vehicle applications.

Other important elements of the code validation process are code-to-code comparisons and numerical tests to check for globally conserved quantities and the effects of numerical parameters and grids on the numerical solution. Some examples of these tests are also discussed. More extensive discussion of such tests can be found in Refs. 3, 5, 7, 22, and 23.

Finally, an example of a flowfield simulation over the full-scale AFE at flight conditions including the effects of thermochemical nonequilibrium is presented. These simulations have been used within the AFE project, in conjunction with other analyses, for heat shield design, aerodynamic coefficient prediction, and the placement and tuning of various experiments. This simulation is also used to test a CSP analysis[18-20] of one of the chemical kinetic models. CSP can be used to identify critical elementary reactions and to simplify the kinetic model. Identification of critical reactions is important because reaction rate expressions are generally extrapolated to high temperatures without benefit of experimental confirmation. Computational chemistry may be used to derive the high, multitemperature functional form of the reaction rate expressions, but such analyses require on the order of one human year for a single reaction. CSP can be used in association with the techniques of computational chemistry to insure that human and computational resources are focused on the most critical reactions.

Aeroassist Flight Experiment—Wind Tunnel

Mach number contours over an AFE model including the sting for Mach 10 flow and $\alpha = -5$ deg are shown in Fig. 1. The Reynolds number for this case is 159,000 based on a model diameter of 9.322 cm. The four-domain grid used for this case is presented in Fig. 2. The grid is composed of 39 transverse by 24 circumferential by 64 normal cells over the

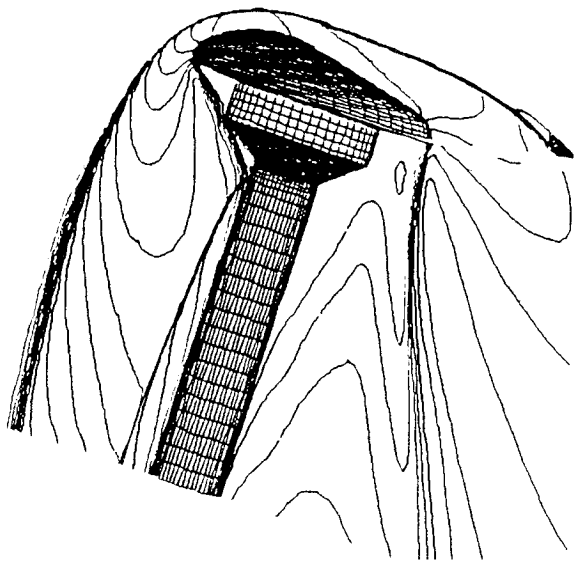

Fig. 1 Mach number contours in the plane of symmetry of the Aeroassist Flight Experiment (AFE) model, including sting, at Mach 10 and Reynolds number of 1.59×10^5.

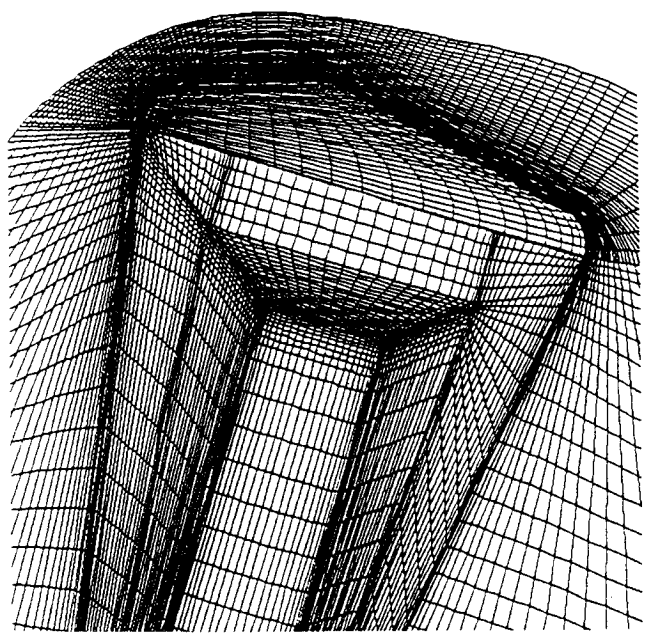

Fig. 2 Multidomain grid defining the surface and plane of symmetry for AFE test case. The domains are approximately divided into forebody, outer wake, shear layer behind the shoulder, and inner wake core surrounding the sting.

forebody, 31 transverse by 24 circumferential by 32 normal cells over the outer base flow, 31 transverse by 24 circumferential by 19 normal cells over the midbase flow region behind the aerobrake, and 26 transverse by 24 circumferential by 21 normal cells over the inner base flow region surrounding the sting. The flow is from top to bottom in the figure. Grid adaption is used over the forebody to align the grid with the captured bow shock. The contours clearly illustrate the sharp, captured bow shock, the captured shock on the wind side of the cylindrical sting, and the free-shear layers emanating behind the circular shoulder of the aerobrake. The multidomain structure facilitates the placement of grid resources to resolve these flow features. However, the free-shear layer behind the left shoulder of the aerobrake turns sharply toward the afterbody, and the present grid appears somewhat coarse in the direction normal to the shear layer.

Comparisons with experimental data[12] for pressure and heat transfer are shown in Fig. 3 on the forebody. Differences between numerical predictions and experiments are generally

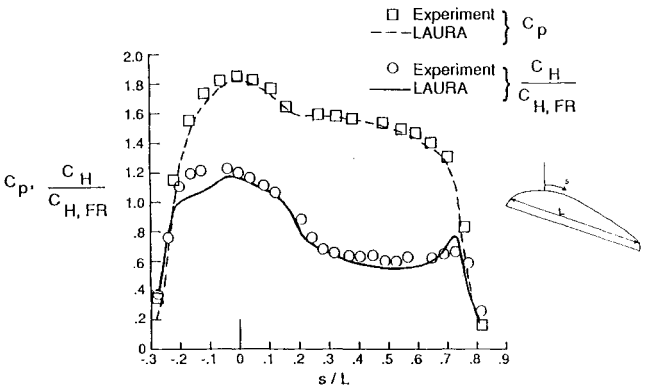

Fig. 3 Comparisons between prediction and experimental data[12] for pressure and heating over the AFE at Mach 10 and $\alpha = 0$ deg.

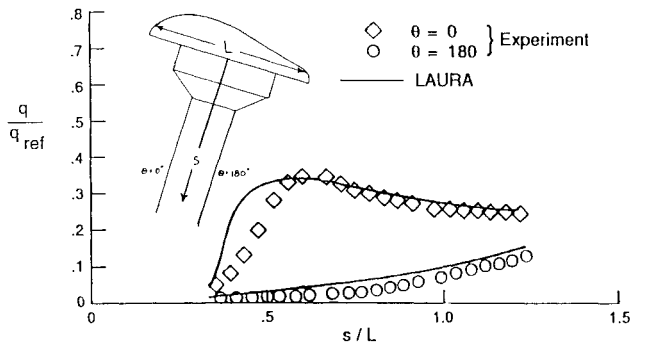

Fig. 4 Comparison between prediction (laminar) and experimental data[13] for heating on sting supporting the AFE model in Mach 10 test case for $\alpha = 0$ deg.

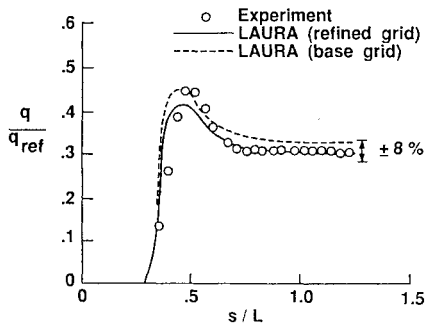

Fig. 5 Comparison between prediction (laminar) and experimental data[13] for heating on sting supporting the AFE model in Mach 10 test case for $\alpha = -5$ deg.

very small and within experimental accuracy, except for the heat transfer in the stagnation region. These differences are believed to be caused by both the varying truncation error behavior as the coordinate singularity in approached from different directions and the predominance of near-zero-valued eigenvalues in the upwind-biased algorithm. There is evidence that the problem is exacerbated by extreme coordinate stretching in the direction normal to the body.

Comparisons with experimental data[13] for heat transfer on the sting are shown in Fig. 4 for $\alpha = 0$ deg and in Fig. 5 for $\alpha = -5$ deg. The comparisons are within experimental accuracy ($\pm 8\%$) on the wind side, except in the intermediate vicinity of the peak heating point where the free-shear layer impacts the sting. The peak heating region is somewhat broadened and may be indicative of the grid spacing described earlier. A grid refinement was implemented to study the possible contributions of grid-induced errors to the magnitude of the sting heating in the $\alpha = -5$ deg case. The number of cells was doubled in the normal direction for all four domains. A slight reduction in predicted heating level is observed, and the prediction is in excellent agreement with the experimental data. The shear layer turning angle can be overpredicted if the grid in the vicinity of the separation point is too coarse. This behavior is believed to be caused by the additional, grid-induced, numerical viscosity, which appears to delay separation, and is consistent with earlier observations using another numerical method in Ref. 24. The accurate prediction of free-shear layer turning angles is important in the design of full-scale aeroassisted space transfer vehicles in order to position the payload in a relatively benign region of the base flow.

Sphere—Ballistic Range

The hypersonic flow over a 1.27-cm-diam sphere in air at Mach number 15.3 ($V_\infty = 5280$ m/s, $T_\infty = 293$ K, $p_\infty = 664$ Pa) is calculated and compared with the experimental data for the shock shape of Lobb[16] and the calculations of Candler[25] using a six-temperature model. The present calculations are made under the assumptions of thermochemical nonequilibrium using a two-temperature model, thermal equilibrium and chemical nonequilibrium, and thermochemical equilibrium. Only seven species were considered in this case in order to be more consistent with Candler's calculations. All of the calculations involving different types of equilibria are made with the same code. The equilibrium calculations are, in fact, approximations to a true equilibrium condition, achieved by increasing the chemical kinetic reaction rate coefficients by a factor of 1×10^6 and by decreasing the characteristic thermal relaxation times by a factor of 1×10^6.

Shock shape calculations are in good agreement with experimental data in Fig. 6. Clearly, both thermal and chemical nonequilibrium must be modeled to agree with the experimental data for the shock shape. The current predictions of the shock shape are approximately 8% below the Candler predictions in the stagnation region and approximately 3% above near the outflow boundary.

Temperature distributions across the shock layer at the stagnation streamline are presented in Fig. 7. Peak translational-rotational temperature behind the shock increases in the presence of chemical and thermochemical nonequilibrium. This behavior is due to the finite accommodation time required for the cascading of translational-rotational energies into the vibrational modes and into the dissociative reactions. The present predictions for translational-rotational and vibrational-electronic temperatures all converge to a single curve in the boundary layer. Chemical nonequilibrium across the shock layer at the stagnation streamline is illustrated in the predictions of NO mass fraction c_{NO} as shown in Fig. 8. The production of NO is primarily a function of the translational-rotational temperature T. Consequently, the distribution of c_{NO} shows the highest peak in the thermochemical nonequilibrium prediction, in which the translational-rotational temperature distribution is the highest. The rather flat distribution of c_{NO}

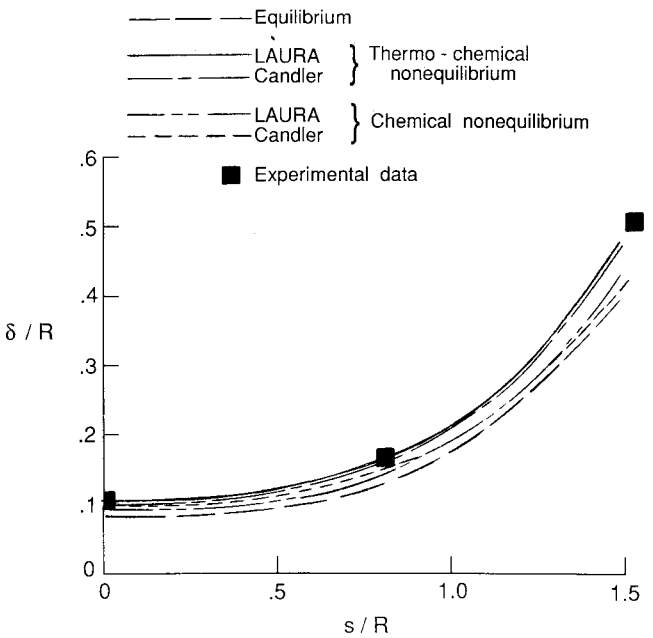

Fig. 6 Nondimensional shock standoff distance vs nondimensional arc length for hypersonic flow over a sphere. Comparisons are made with experimental data of Lobb[16] and calculations of Candler.[25]

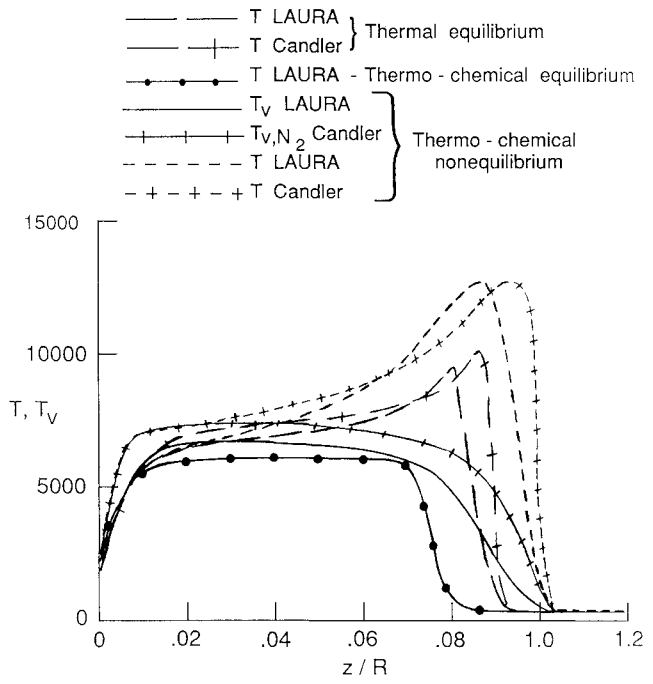

Fig. 7 Temperature distributions across shock layer under assumptions of thermochemical nonequilibrium, thermal equilibrium and chemical nonequilibrium, and thermochemical equilibrium.

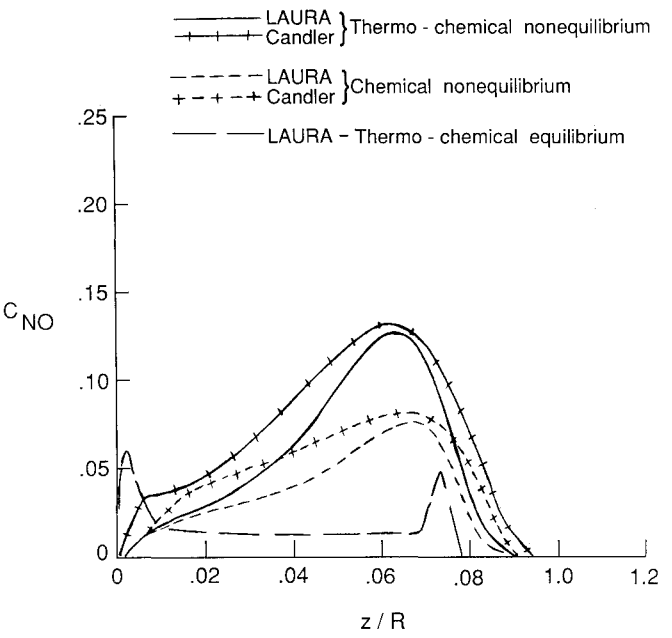

Fig. 8 Mass fraction distribution of NO across shock layer under assumptions of thermochemical nonequilibrium, thermal equilibrium and chemical nonequilibrium, and thermochemical equilibrium.

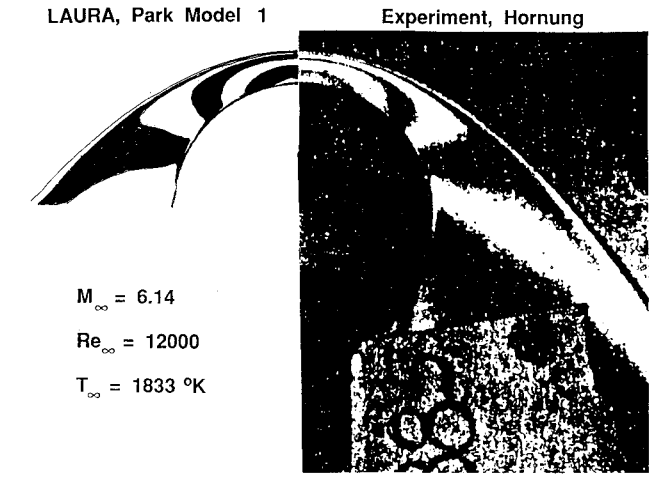

Fig. 9 Calculated and experimental[17] fringe patterns over cylinder in partially dissociated nitrogen obtained in shock tunnel using chemical kinetic model of Park.

under conditions of thermochemical equilibrium is indicative of the flat temperature distribution across the inviscid portion of the shock layer. The increase in c_{NO} in the boundary layer highlights the importance of three-body recombination, which becomes significant as the equilibrium state is approached. The peak value of c_{NO} in the captured shock corresponds to local conditions within the shock transition zone. The grid is too coarse and the Navier-Stokes equations are inadequate to accurately predict flow quantities within the captured shock.

The near-equilibrium calculation is subject to instabilities associated with the stiffness of the governing equations. Starting from a converged chemical nonequilibrium solution, the error norm for this case quickly dropped eight orders of magnitude in 1000 iterations, but suddenly jumped three orders of magnitude, at which point the error norm thrashed about a constant level. A check for elemental mass fraction along the stagnation streamline, which should be constant for this case, revealed a 12% maximum error in oxygen fraction in the boundary layer, near the local maximum value for c_{NO}. Mass fraction conservation above the boundary layer was good, with average errors in oxygen fraction less than 1%, and the postshock values of temperature and species mass fraction are in good agreement with equilibrium, normal shock theory.

Cylinder—Shock Tunnel

The flow around a 5.08-cm-diam cylinder in high temperature, partially dissociated nitrogen was computed, and fringe patterns are compared to the interferograms obtained by Hornung.[17] Freestream conditions for this case are $V_\infty = 5.59$ km/s, $T_\infty = 1833$ K, $c_{N_2} = 0.927$, and $c_N = 0.073$. The fringe number F is determined by the expression

$$F = \frac{\Delta\rho L(1 + c_N)}{4160\lambda} \tag{6}$$

where λ is the wavelength and L is the geometrical path, taken here as the cylinder length equal to 0.1524 m (6 in.). No attempt was made to account for changes in the geometric path through the shock envelope due to three-dimensional effects at the edge of the cylinder. Calculated and experimental fringe patterns in which the chemical kinetic model is due to Park, as described in Ref. 5, are compared in Fig. 9. A recent revision of this data set (Park, private communication of lecture notes) was also tested, and the associated computation is compared to experiment in Fig. 10. The reactions in question are given by

$$N_2 + N_2 \rightarrow N + N + N_2$$

$$N_2 + N \rightarrow N + N + N$$

The forward (endothermic) reaction rate coefficient for reaction r is given by

$$k_{f,r} = C_r T_d^{-1.6} e^{\frac{-113{,}200}{T_d}} \tag{7}$$

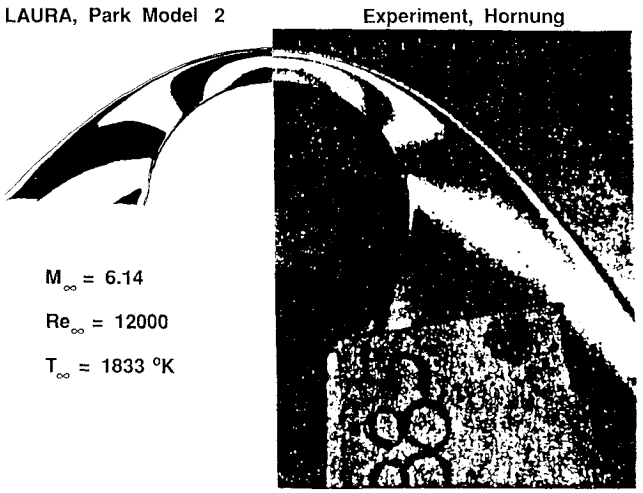

Fig. 10 Calculated and experimental[17] fringe patterns over cylinder in partially dissiociated nitrogen obtained in shock tunnel using revised chemical kinetic model of Park.

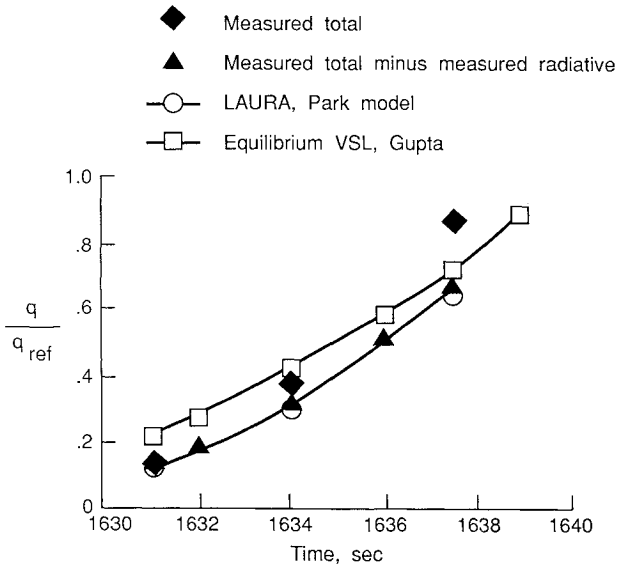

Fig. 11 Stagnation-point, convective, heating predictions compared to experimental data for the Fire II flight test[14] during early period in which radiative heating levels were small and thermochemical nonequilibrium effects were significant.

where $C_{r1} = 3.7 \times 10^{21}$ and $C_{r2} = 1.6 \times 10^{22}$ in the original model and $C_{r1} = 7.0 \times 10^{21}$ and $C_{r2} = 3.0 \times 10^{22}$ in the revised model. In all cases, $T_d = (TT_V)^{1/2}$ is used as the rate-controlling temperature for dissociative reactions.

Both cases are in reasonably good agreement with the experimental data. Neither is an exact match. The differences in the fringe patterns due to changes in the kinetic model are apparent in the stagnation region, and the revised model may be slightly better agreement with the data in this region. However, some shifting in fringe patterns can also be induced using different interpretations of the variation of L across the shock layer. Consequently, this comparison should be considered more of a qualitative check of the thermochemical model and not used to deduce reaction rate coefficients.

The calculated shock shape is in excellent agreement with the experimental data. A thermal equilibrium, chemical nonequilibrium case was run by reducing the characteristics time for vibrational relaxation by a factor of 10^5. The change in shock standoff distance at the stagnation streamline was less than 5% as compared to the thermochemical nonequilibrium case. This result is in contradiction with the earlier calculations of Candler,[25] which showed a 50% reduction in shock standoff distance under the assumption of thermal equilibrium.

Fire II Stagnation Point Heating—Flight Data

Fire II flight data[14] consist of measured total heating rates (convective plus absorbed radiative), radiative intensity in the 0.2–6.2 eV range, and spectral radiation in the 2.0–4.0 eV range. Only the stagnation point measurements are examined in the present set of results. The vehicle was constructed with a layered heatshield consisting of three beryllium layers. The vehicle had a truncated, hemispherical shape with a small corner radius. The calculations were performed at three points during the early data period on the first heatshield, which is characterized by low radiation and significant thermochemical nonequilibrium. A fully catalytic wall boundary condition is assumed. An equivalent sphere geometry was defined as in Refs. 26–28 with a nose radius of 0.747 m. The freestream velocity equals 11.3 km/s, and the altitude range covered by this early data period was between 84.6–67.05 km. The calculated convective heating rates from LAURA are compared to the equilibrium viscous shock-layer results of Ref. 28 and to the experimental data in Fig. 11. The predictions are in excellent agreement with the total heating data at the earliest data point, at which time there was no significant radiative heating. A crude approximation to the actual convective heating rate is deduced from measured quantities by subtracting the measured radiative heating in the 0.2–6.2 eV range from the measured total heating. This approximation ignores radiation outside of the measured range and does not account for the actual absorbtivity of the beryllium heatshield. The inferred experimental convective heating is in good agreement with the LAURA predictions, but this agreement is of dubious significance at the later data period ($t = 1637.5$ s). Of greater significance is the convergence of the equilibrium and nonequilibrium predictions at the lower altitudes using two different approaches that provide independent checks of the predicted convective heating.

RAM-C III Electron Number Densities—Flight Data

A series of flight tests conducted on a 9-deg, spherically capped cone to measure electron number density across the shock layer are described in Refs. 15 and 29. Microwave reflectometers were used to measure the peak values of electron number densities in the shock layer at several locations along the cone. A Langmuir probe rake that extended across the shock layer at the base of the cone measured electron number density profiles. A schematic of the vehicle and experiment locations is shown in Fig. 12.

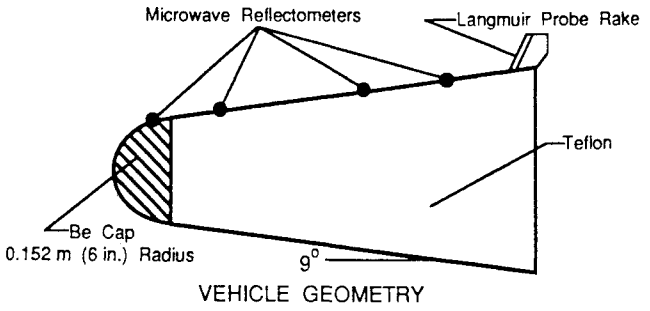

Fig. 12 Schematic of RAM-C test vehicle and location of experiments.

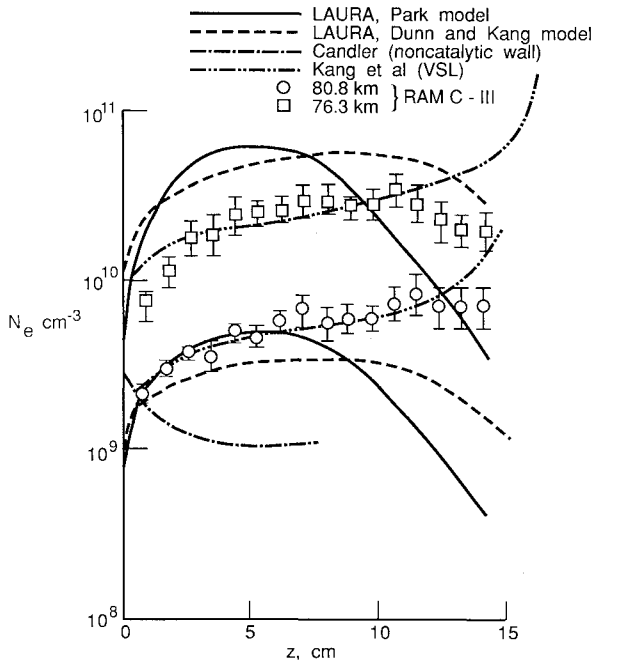

Fig. 13 Experimental and numerical profiles of electron number density across shock layer of RAM-C III vehicle. Comparisons are also made with calculations of Kang et al.[15] and Candler and MacCormack.[31]

Comparisons were made with the data at three trajectory points (80.8, 76.3, and 71.0 km) at a freestream velocity equal to 7.65 km/s. Experimental and numerical data for electron number density profiles across the shock layer at the base are shown in Fig. 13. Experimental and numerical data for peak electron number density along the shock layer are compared in Fig. 14. The LAURA predictions were implemented using two different chemical kinetic models, as described in Ref. 5. The profile shapes given by the Dunn and Kang chemical kinetic model appear to be in better qualitative agreement with the experimental profiles than the Park model, though both predictions are in poor quantitative agreement with experiment. Predictions are somewhat low at the highest altitude (80.8 km) but are progressively higher than experiment as altitude is decreased. Both predicted profile shapes drop off as the captured shock is approached; the tendency is, however, more severe with the Park model. It is believed that this rapid drop in number density is a consequence of empirical and numerical phenomena. First, ionization is a strong function of T_V in the two-temperature model. Because T_V tends to be low behind the captured shock, ionization may be inhibited if the empirical dependence is too strong. Second, numerical dissipation of electrons across the captured shock can be significant if the grid is too coarse. This behavior is discussed in more detail in Ref. 5.

Single-temperature, shock-fitted viscous shock-layer (VSL) methods show much better agreement with the experimental

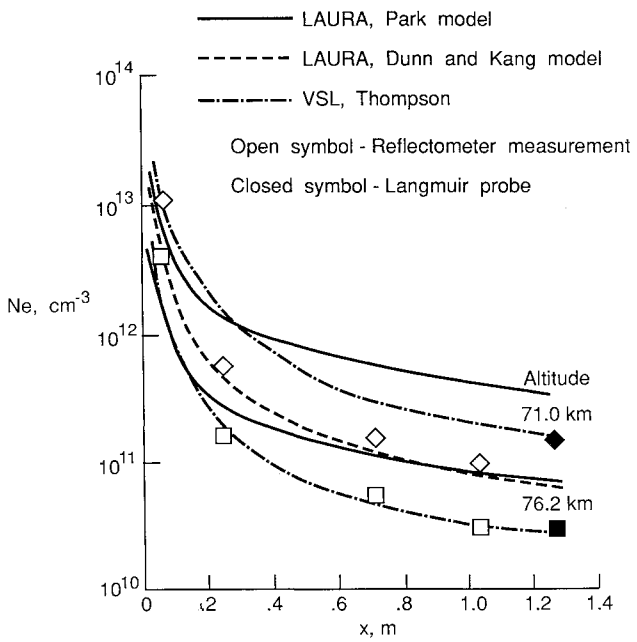

Fig. 14 Experimental and numerical distributions of peak values of electron number densities within the shock layer along the RAM-C III vehicle. Comparisons are also made with calculations of Thompson using a VSL code derived from Ref. 30.

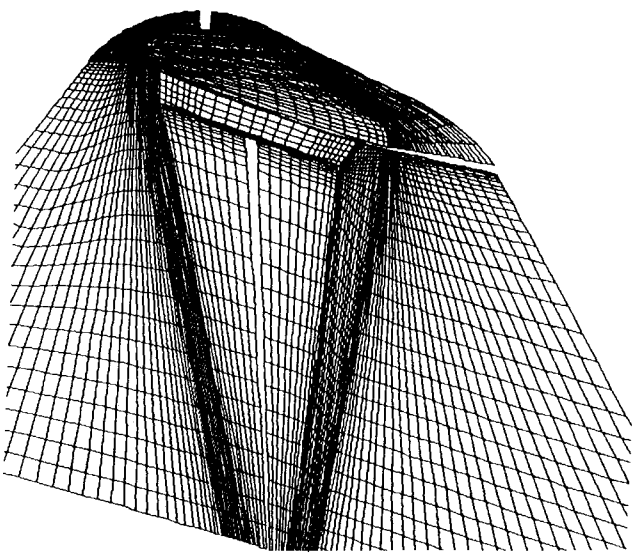

Fig. 15 Multidomain grid defining the plane of symmetry for AFE flight case. The domains are approximately divided into forebody, outer wake, shear layer behind the shoulder, and inner wake core.

data than the present method. For example, the results of Kang et al.[15] are in substantially better agreement with experiment than the LAURA results. This method assumes species are frozen across the fitted shock, and postshock temperatures are considerably higher under this assumption. Thompson's results (private communication) are based on VSL code[30] that uses shock slip boundary conditions to further improve both profile shapes and peak number density values (see Fig. 14) as compared to experiment. The only other multitemperature shock-capturing method compared with this data set is that of Candler and MacCormack,[31] as shown in Fig. 13. This method used a noncatalytic wall boundary condition, which moves the peak number density prediction to the wall. The other calculations used fully catalytic wall boundary conditions. Much work remains to be done with regard to the thermochemical nonequilibrium simulations of electron number density profiles utilizing multitemperature shock-capturing methods. The

first task is to perform a more rigorous grid refinement study for this case.

AFE—Flight Simulation

The four-domain grid used for the investigation of hypersonic flow over the AFE in both chemical and thermal nonequilibrium at 8917 m/s and 78 km altitude is shown in Fig. 15. All 11 species are included in this calculation. The multidomain grid allows for better resolution of the free-shear layer coming off the shoulder as compared with the resolution that can be achieved using a single-domain structured grid. The forebody shape is composed of an elliptic nose, a raked elliptic cone, and a circular shoulder. The afterbody carrier vehicle is a hexagonal cross section block. Grid lines on the surface are shown in subsequent figures.

Contours for translational temperature, vibrational temperature, Mach number, and electron number density are shown in Figs. 16–19. These contour lines, which are monochrome versions of a color-coded figure, serve to qualitatively define the flow structure. Note that contour lines continue smoothly over domain boundaries. The gaps between domains are an artifact of the cell-centered structure of the data sets. The boundaries of the domains coincide, but there is a gap between cell centers.

The flow is from top to bottom in the figures. Both the bow shock wave and the free-shear layer structure are well defined in these figures. Also observe that the vibrational temperature and electron number density tend to stay frozen in the shear layer coming off the shoulder of the vehicle. Peak translational temperature is approximately 22,000 K in a thermal relaxation zone, which encompasses nearly one-fourth of the shock-layer thickness. Peak vibrational temperature in this region is approximately 10,000 K. In contrast, the vibrational temperature in much of the wake core is approximately 4000 K, whereas the translational temperature is below 2000 K. The domain of the wake core is shown in Fig. 18, which illustrates the extent of the subsonic region. Note that the lower left corner of the hexagonal carrier juts into the subsonic portion of the free-shear layer. Present calculations show enhanced convective heating at this point relative to typical heating levels elsewhere on the carrier.

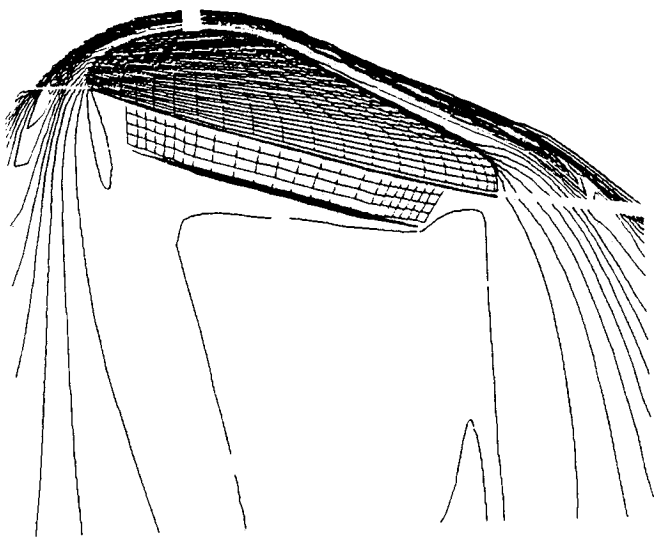

Fig. 16 Translational temperature contours of flow over AFE at 8917 m/s and 78 km altitude.

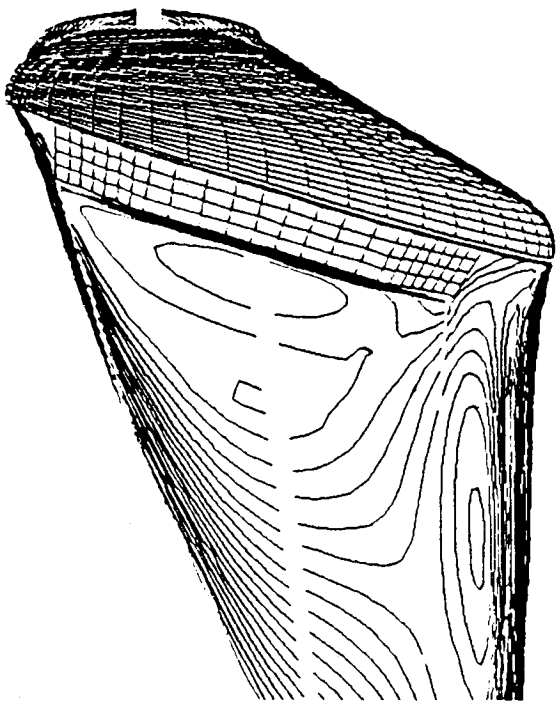

Fig. 18 Mach number contours showing the subsonic region for flow over AFE at 8917 m/s and 78 km altitude.

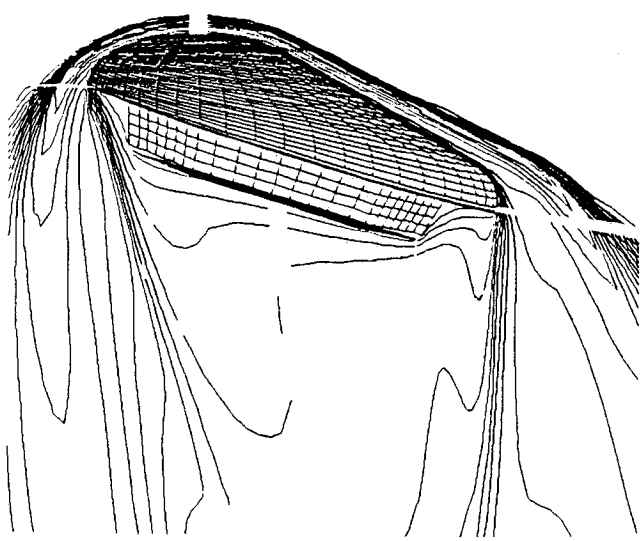

Fig. 17 Vibrational temperature contours for flow over AFE at 8917 m/s and 78 km altitude.

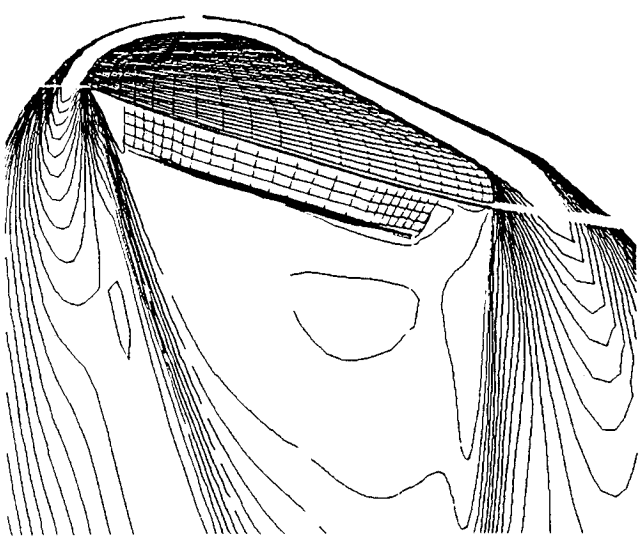

Fig. 19 Electron number density contours for flow over AFE at 8917 m/s and 78 km altitude.

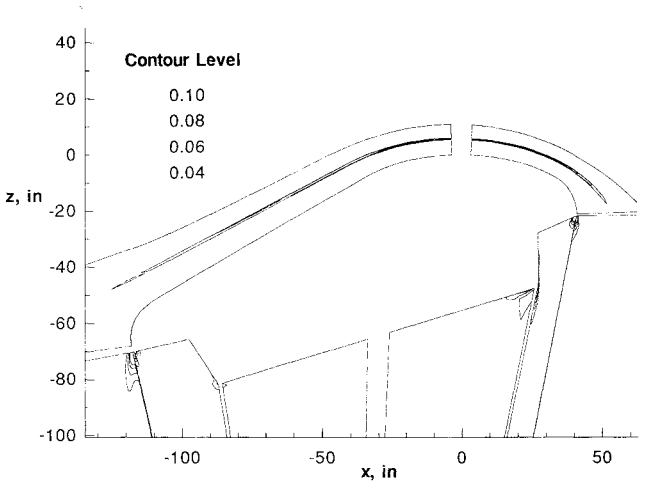

Fig. 20 Contour plot of Knudsen number in the plane of symmetry of AFE flight case corresponding to $V_\infty = 9.326$ km/s, $\rho_\infty = 4.293 \times 10^{-5}$ kg/m^3, and $T_\infty = 200$ K at an altitude of 75.2 km and $\alpha = -5$ deg. The maximum value exceeds 1.0 immediately behind the expansion corner.

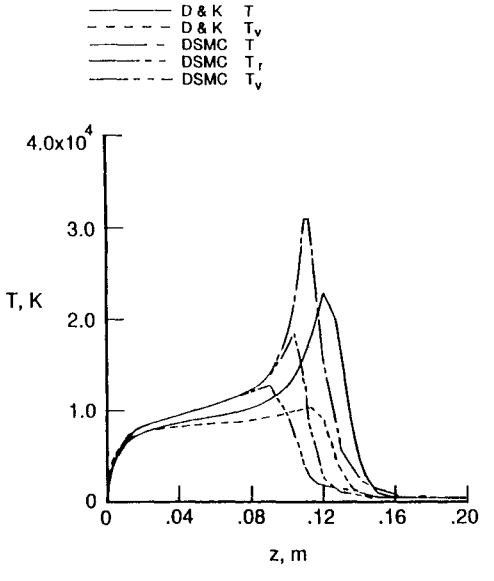

Fig. 21 Temperature profile predictions across stagnation streamline for noncontinuum, direct simulation Monte Carlo algorithm, and continuum LAURA algorithm.

The AFE flowfield was computed using a steady, laminar, thin-layer approximation in three dimensions. This approximation yields the Navier-Stokes equations minus the cross-derivative viscous terms in computational space. Also, computed Knudsen numbers in the base flow (i.e., the ratio of mean free path to local characteristic length) are as large as 1.0 in the low-density region immediately behind the shoulder. The local characteristic length is equal to $\rho / |\nabla \rho|$ and gives an approximation of the length scale over which significant changes in the flowfield are accommodated. The continuum approximation begins to break down when the Knudsen number is of order 1 or larger. A representative Knudsen number contour plot in the plane of symmetry is shown in Fig. 20. This case corresponds to freestream conditions given by $V_\infty = 9.326$ km/s, $\rho_\infty = 4.293 \times 10^{-5}$ kg/m^3, and $T_\infty = 200$ K at an altitude of 75.2 km and $\alpha = -5$ deg. A recently computed case earlier in the simulated AFE trajectory at a higher altitude ($V_\infty = 9.863$ km/s, $\rho_\infty = 5.682 \times 10^{-6}$ kg/m^6, and $T_\infty = 189$ K at an altitude of 87.3 km and $\alpha = 0$ deg) revealed order 1 Kundsen numbers in the captured shock and a larger region of order 1 values behind the corners of the aerobrake. Simulation errors

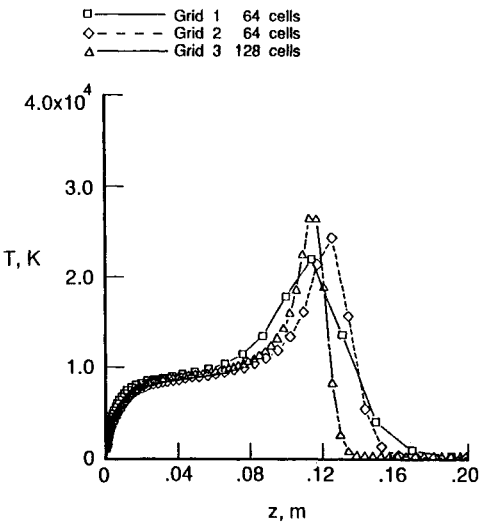

Fig. 22 Temperature profile predictions across stagnation streamline with three different grids for axisymmetric AFE.

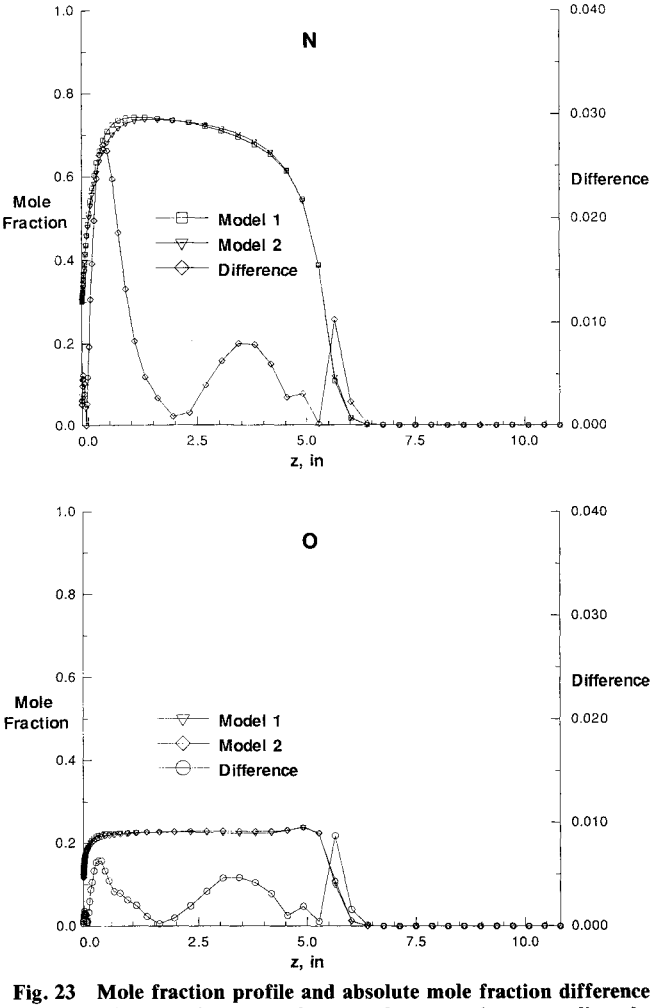

Fig. 23 Mole fraction profile and absolute mole fraction difference for the major constituent species near the stagnation streamline obtained using the full chemical kinetic model of Dunn and Kang and a simplified model defined by computational singular perturbation (CSP) for AFE flight case defined in Fig. 20.

due to the limitations of the present equation set in these isolated areas of large Knudsen numbers require more study. One element of this study follows.

Comparisons with Direct Simulation Monte Carlo

An axisymmetric approximation to the AFE was used to compare computed results using LAURA and a direct simulation Monte Carlo (DSMC) algorithm.[32] The DMSC code uses a kinetic-theory-based particle simulation approach to hypersonic, rarefied-flow analysis. As with any approximation scheme, the DSMC approach is also subject to physical modeling errors, particularly with regard to the description of reacting gases. However, the DSMC method is better at describing low-density flows, and it requires no a priori assumptions concerning the evaluation of dissipative phenomena as required in the Navier-Stokes approximation.

Comparisons of predicted temperatures across the shock layer of the axisymmetric AFE from LAURA using the Dunn and Kang chemical kinetic model and DSMC are presented in Fig. 21. The DSMC results show separate translational, rotational, and vibrational temperatures, whereas the LAURA results assume the two-temperature approximation. The peak translational-rotational temperature from the LAURA prediction falls between the translational and rotational peaks of the DSMC prediction. Shock standoff distance, as judged by the location of the peak translational temperature, is in good agreement between the two methods. The thickness of the shock transition zone is in fair agreement as judged by the temperature profiles. However, this agreement may be misleading. More extensive comparisons presented in Ref. 5 reveal thicker shock transition zones as measured by the species mole fraction profiles. Also, at higher altitudes, the Navier-Stokes predictions show sharper, narrower profiles across the shock transition zone as compared to DSMC.

The thickness of the computed shock transition zone can also be affected by grid resolution across the captured shock. The effects of grid resolution are illustrated in Fig. 22 for translational temperature profiles across the stagnation streamline. Grids 1 and 2 are made up of 64 cells, which are exponentially stretched from the body to the inflow boundary ahead of the shock. Grid 1 has a minimum cell size at the wall equal to the 2.872×10^{-6} m and an average cell size through the shock transition zone equal to 1.5×10^{-2} m. Grid 2 has a minimum cell size at the wall equal to 1.05×10^{-4} m and an average cell size through the shock transition zone equal to 8.0×10^{-3} m. Grid 3 is made up of 128 exponentially stretched cells with a minimum cell size at the wall equal to 5.12×120^{-5} m and an average cell size through the shock transition zone equal to 4.0×10^{-5} m. The ratio of mean free path to cell size (cell Knudsen number) based on conditions at the beginning of the shock transition zone equals 0.193 for grid 1, 0.363 for grid 2, and 0.725 for grid 3. The actual distribution of mesh points across the shock layer is indicated by the symbol location in Fig. 22.

Figure 22 shows a sharper, higher peak in the translational temperature as the grid is refined across the captured shock. This trend is similar to one obtained in Ref. 33 in a simulation of the effects of a relatively coarse grid resolution of reacting flow crossing a normal shock through the use of artificial viscosity. The thickness of the peak (thermal and chemical relaxation zone) for grid 3 is approximately equal to the DSMC results in Fig. 21. Further refinement would probably sharpen the peak a little more, but it is not clear that cell averages taken over a dimension less than the local mean free path would be physically meaningful. More details of the grid refinement study are also presented in Ref. 5.

Computational Singular Perturbation Simplification of the Chemical Kinetic Model

CSP[18-20] was used to simplify the Dunn and Kang chemical kinetic model used in the calculation of the forebody AFE flowfield at 75.2 km described earlier. The Dunn and Kang model[34] consists of 26 reaction pairs (52 forward and backward reactions). This full set is identified as model 1 in Fig. 23. Data for T, T_V, and the 11 species number densities at seven points distributed across the shock layer near the stagnation streamline were used to define a participation index for each of the 52 elementary reactions using CSP. The participation index provides a measure of the dependence of species number density evolution on an individual reaction. Reactions with a participation index less than 0.2 at the seven test locations were eliminated from the model. The reduced model, identified as model 2 in Fig. 23, consists of 27 reactions.

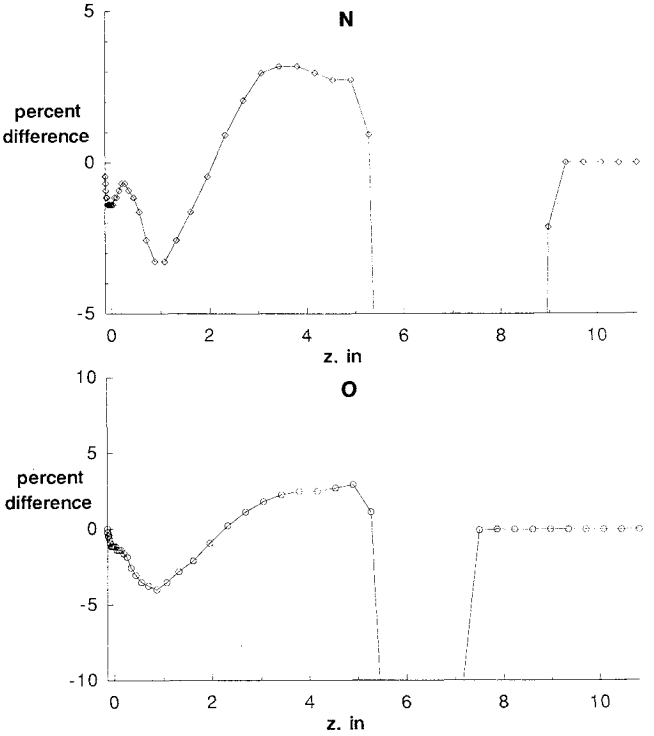

Fig. 24 Percent difference of number densities for AFE flight case as computed using the complete chemical kinetic model of Dunn and Kang and a simplified model defined by CSP. Percent difference is measured with respect to the complete model.

Figure 23 shows the mole fraction profile across the shock layer and the absolute value of the mole fraction difference between the two models for the predominant species in the shock layer. Figure 24 shows the associated percent difference of the predicted number density relative to model 1. The two models are in very good agreement. In Fig. 23 the largest difference in mole fraction in any of the species is less than 0.04. The percent differences in Fig. 24 tend to be large (greater than 20%) in high gradient regions. These differences may be attributed as much to numerical dissipation in high gradient regions as to differences in the chemical kinetic models.

The major benefit of CSP is to define alternatives and equivalent representations of the chemical kinetic model, which identify partial equilibrium relationships and remove the potential problems associated with stiff systems of equations. LAURA is not yet set up to utilize the alternative representations defined by CSP. However, the good comparisons between the full and reduced model calculations, as based on the participation index of the CSP analysis, provide practical verification of the validity of CSP for AFE flowfield applications.

Concluding Remarks

The code calibration program for the Langley Aerothermodynamic Upwind Relaxation Algorithm (LAURA) is reviewed, with emphasis directed toward support of the Aeroassist Flight Experiment (AFE). The flight project is de-

signed to obtain data that will be used in the validation of computational fluid dynamic approximation methods. Comparisons between experimental data and numerical solution focus on perfect-gas tests over a scale model of the AFE and on flight and ground tests that challenge some aspect of the thermochemical nonequilibrium model. In the first case, the gas model is simple, but the grid-related problems of defining the real vehicle are present. In the second case, the vehicle geometries are simple, but thermochemical processes must be modeled correctly in order to compare with the experimental data. These comparisons are described as calibration runs because they test elements of the numerical solution, but no single data set adequately simulates the full-scale AFE flight conditions.

Perfect-gas flow predictions featured comparisons to experimental data for pressures and heating on the forebody of the AFE and on sting heating. Comparisons are generally very good. Problems with grid singularity induced truncation errors create some difficulties in stagnation region heating predictions. The multidomain grid facilitates the placement of grid resources to resolve the free-shear layer coming off the corner of the aerobrake. The agreement with experimental data for sting heating is good and demonstrates the ability of the code to predict shear layer turning angles. The accurate prediction of free-shear layer turning angles is important in the design of full-scale aeroassisted space transfer vehicles in order to position the payload in a relatively benign region of the base flow.

Aspects of the thermochemical nonequilibrium model are challenged by two ground-based tests in a ballistic range and a shock tunnel. Experimental data for shock shape are in good agreement with the present calculations in the first test. Interferograms appear to be in reasonably good qualitative agreement in the second case. Sample calculations involving variations in the thermochemical nonequilibrium model reveal the magnitude of the contributions of various aspects of the model. Code-to-code comparisons are also used in the verification of the present computations.

Flight-test data consitute the final calibration data set. Predictions in stagnation point convective heating are in very good agreement with the Fire II data set, taken early in the trajectory when radiative heating was low and thermochemical nonequilibrium effects were significant. Comparisons to the RAM-C III data set for electron number density in the shock layer of a 9-deg spherically blunted cone are poor. In general, fitted shock analysis techniques are in better agreement with the experimental data. Differences may be a function of the empirical dependence of the ionization reactions on the vibrational-electronic temperature T_V and on excessive dissipation across the captured shock.

An example of flowfield simulation over the full-scale AFE is discussed. The importance of thermal nonequilibrium in the flowfield is highlighted. Limitations of the simulation caused by the magnitude of the Knudsen number in isolated regions of the flow are also discussed, though no quantitative assessment of the simulation can be offered at this time. Some of the limitations are addressed in comparisons with a direct simulation Monte Carlo, kinetic-theory-based flow simulation and in a grid refinement study.

This simulation is also used to test a computational singular perturbation (CSP) analysis of one of the chemical kinetic models. CSP can be used to identify critical elementary reactions and to simplify the kinetic model. Identification of critical reactions is important because reaction rate expressions are generally extrapolated to high temperatures without benefit of experimental confirmation. Computational chemistry may be used to derive the high, multitemperature functional form of the reaction rate expressions, but such analyses require on the order of one human year for a single reaction. CSP can be used in association with the techniques of computational chemistry to insure that human and computational resources are focused on the most critical reactions.

Acknowledgments

The author thanks Dimitri Goussis of Princeton University for running the computational singular perturbation analysis of the Aeroassist Flight Experiment flowfield data set.

References

[1]Jones, J. J., "The Rationale for an Aeroassist Flight Experiment," AIAA Paper 87-1508, June 1987.

[2]Walberg, G. D., "A Survey of Aeroassisted Orbit Transfer," *Journal of Spacecraft and Rockets*, Vol. 22, No. 1, 1985, pp. 3-18.

[3]Gnoffo, P. A., "Application of Program LAURA to Three-Dimensional AOTV Flowfields," AIAA Paper 86-0565, Jan. 1986.

[4]Gnoffo, P. A., McCandless, R. S., and Yee, H. C., "Enhancements to Program LAURA for Computation of Three-Dimensional Hypersonic Flow," AIAA Paper 87-0280, Jan. 1987.

[5]Gnoffo, P. A., Gupta, R. N., and Shinn, J., "Conservation Equations and Physical Models for Hypersonic Air Flows in Thermal and Chemical Nonequilibrium," NASA TP-2867, Feb. 1989.

[6]Gnoffo, P. A., "Upwind-Biased, Point-Implicit Relaxation Strategies for Viscous, Hypersonic Flows," AIAA Paper 89-1972, June 1989.

[7]Gnoffo, P. A., "An Upwind, Point-Implicit Relaxation Algorithm for Viscous, Compressible Perfect-Gas Flows," NASA TP (in review).

[8]Roe, P. L., "Approximate Riemann Solvers, Parameter Vectors, and Difference Schemes," *Journal of Computational Physics*, Vol. 43, No. 2, 1981, pp. 357-372.

[9]Harten, A., "High Resolution Schemes for Hyperbolic Conservation Laws," *Journal of Computational Physics*, Vol. 49, No. 3, 1983, pp. 357-393.

[10]Yee, H. C., "On Symmetric and Upwind TVD Schemes," NASA TM-86842, Sept. 1985.

[11]Yee, H. C., "Numerical Experiments with a Symmetric High-Resolution, Shock-Capturing Scheme," NASA TM-88325, June 1986.

[12]Micol, J. R., "Experimental and Predicted Pressure and Heating Distributions for an Aeroassist Flight Experiment Vehicle in Air at Mach 10," AIAA Paper 89-1731, June 1989.

[13]Wells, W. L., "Measured and Predicted Aerodynamic Heating on a Cylinder in Wake of AFE Configuration at Incidence," AIAA Paper 89-2162, July 1989.

[14]Cauchon, D. L., "Radiative Heating Results from the Fire II Flight Experiment at a Reentry Velocity of 11.4 Kilometers per Second," NASA TM X-1402, 1966.

[15]Kang, S.-W., Jones, W. L., and Dunn, M. G., "Theoretical and Measured Electron Density Distributions at High Altitudes," *AIAA Journal*, Vol. 11, No. 2, 1973, pp. 141-149.

[16]Lobb, R. K., "Experimental Measurement of Shock Detachment Distance on Spheres Fired in Air at Hypervelocities," *The High Temperature Aspects of Hypersonic Flow*, edited by W. C. Nelson, Pergammon, New York, 1964.

[17]Hornung, H. G., "Non-equilibrium Dissociating Nitrogen Flow Over Spheres and Circular Cylinders," *Journal of Fluid Mechanics*, Vol. 53, Pt. 1, 1972, pp. 149-176.

[18]Lam, S. H., Goussis, D. A., and Konopka, D., "Time-Resolved Simplified Chemical Kinetics Modelling Using Computational Singular Perturbation," AIAA Paper 89-0575, Jan. 1989.

[19]Lam, S. H., and Goussis, D. A., "Basic Theory and Demonstrations of Computational Singular Perturbation for Stiff Equations," *Proceedings of the 12th IMACS World Congress on Scientific Computation*, July 1988.

[20]Lam, S. H., and Goussis, D. A., "Understanding Complex Chemical Kinetics with Computational Singular Perturbation," Dept. of Mechanical and Aerospace Engineering, Princeton Univ., Princeton, NJ, MAE Rept. 1799, Jan. 1988.

[21]Park, C., "Assessment of Two-Temperature Kinetic Model for Ionizing Air," AIAA Paper 87-1574, June 1987.

[22]Rudy, D. H., Kumar, A., Thomas, J., Gnoffo, P. A., and Chakravarthy, S. R., "A Comparative Study and Validation of Upwind and Central-Difference Navier-Stokes Codes for High Speed Flows," AGARD Symposium on Validation of Computational Fluid Dynamics, Lisbon, Portugal, CP 437, May, 1988, pp. 37-1 to 37-15.

[23]Rudy, D. H., Thomas, J., Kumar, A., Gnoffo, P. A., and Chakravarthy, S. R., "A Validation Study of Four Navier-Stokes Codes for High Speed Flows," AIAA Paper 89-1838, June 1989.

[24]Gnoffo, P. A., "Complete Flowfields Over Low and Wide Angle AOTV Conceptual Configurations," AIAA Paper 84-1695, June 1984.

[25]Candler, G., "On the Computation of Shock Shapes in Nonequilibrium Hypersonic Flows," AIAA Paper 89-0312, Jan. 1989.
[26]Sutton, K., "Air Radiation Revisited," AIAA Paper 84-1733, June 1984.
[27]Zoby, E. V., and Sullivan, E. M., "Effects of Corner Radius on Stagnation-Point Velocity Gradients on Blunt, Axisymmetric Bodies," NASA TM X-1067, March 1965.
[28]Gupta, R. N., "Navier-Stokes and Viscous Shock-Layer Solutions for Radiating Hypersonic Flows," AIAA Paper 87-1576, June 1987.
[29]Jones, W. L., and Cross, A. E., "Electrostatic Probe Measurements of Plasma Parameters for Two Re-entry Flight Experiments at 25,000 ft/sec," NASA TN D-6617, April 1972.
[30]Swaminathan, S., Kim, M. D., and Lewis, C. H., "Three-Dimensional Nonequilibrium Viscous Shock-Layer Flows Over Complex Geometries," AIAA Paper 83-0212, Jan. 1983.
[31]Candler, G. V., and MacCormack, R. W., "The Computation of Hypersonic Ionized Flows in Chemical and Thermal Nonequilibrium," AIAA Paper 88-0511, Jan. 1988.
[32]Moss, J. N., Bird, G. A., and Dogra, V. K., "Nonequilibrium Thermal Radiation for an Aeroassist Flight Experiment Vehicle," AIAA Paper 88-0081, Jan. 1988.
[33]Macaraeg, M. G., and Street, C. L., "An Analysis of Artificial Viscosity Effects on Reacting Flows Using a Spectral Multi-Domain Technique," *Computational Fluid Dynamics*, edited by G. de Vahl and C. Fletcher, Elseveir Science, 1988, pp. 503–514.
[34]Dunn, M. G., and Kang., S.-W., "Theoretical and Experimental Studies of Reentry Plasmas," NASA CR-2232, April 1973.

Clark H. Lewis
Associate Editor

Recommended Reading from the AIAA Progress in Astronautics and Aeronautics Series . . . AIAA

Opportunities for Academic Research in a Low-Gravity Environment

George A. Hazelrigg and Joseph M. Reynolds, editors

The space environment provides unique characteristics for the conduct of scientific and engineering research. This text covers research in low-gravity environments and in vacuum down to 10^{-15} Torr; high resolution measurements of critical phenomena such as the lambda transition in helium; tests for the equivalence principle between gravitational and inertial mass; techniques for growing crystals in space—melt, float-zone, solution, and vapor growth—such as electro-optical and biological (protein) crystals; metals and alloys in low gravity; levitation methods and containerless processing in low gravity, including flame propagation and extinction, radiative ignition, and heterogeneous processing in auto-ignition; and the disciplines of fluid dynamics, over a wide range of topics—transport phenomena, large-scale fluid dynamic modeling, and surface-tension phenomena. Addressed mainly to research engineers and applied scientists, the book advances new ideas for scientific research, and it reviews facilities and current tests.

TO ORDER: **Write, Phone, or FAX:** AIAA c/o TASCO,
9 Jay Gould Ct., P.O. Box 753, Waldorf, MD 20604
Phone (301) 645-5643, Dept. 415 ■ FAX (301) 843-0159

Sales Tax: CA residents, 7%; DC, 6%. For shipping and handling add $4.75 for 1–4 books (call for rates for higher quanties). Orders under $50.00 must be prepaid. Foreign orders must be prepaid. Please allow 4 weeks for delivery. Prices are subject to change without notice. Returns will be accepted within 15 days.

1986 340 pp., illus. Hardback
ISBN 0-930403-18-5
AIAA Members $59.95
Nonmembers $84.95
Order Number V-108